



HAL
open science

Effect of rising motion on the damped shape oscillations of drops and bubbles

Benjamin Lalanne, Sébastien Tanguy, Frédéric Risso

► **To cite this version:**

Benjamin Lalanne, Sébastien Tanguy, Frédéric Risso. Effect of rising motion on the damped shape oscillations of drops and bubbles. *Physics of Fluids*, 2013, vol. 25, pp. 1-22. 10.1063/1.4829366 . hal-00946159

HAL Id: hal-00946159

<https://hal.science/hal-00946159>

Submitted on 13 Feb 2014

HAL is a multi-disciplinary open access archive for the deposit and dissemination of scientific research documents, whether they are published or not. The documents may come from teaching and research institutions in France or abroad, or from public or private research centers.

L'archive ouverte pluridisciplinaire **HAL**, est destinée au dépôt et à la diffusion de documents scientifiques de niveau recherche, publiés ou non, émanant des établissements d'enseignement et de recherche français ou étrangers, des laboratoires publics ou privés.



This is an author-deposited version published in: <http://oatao.univ-toulouse.fr/>
Eprints ID : 10913

To link to this article : DOI: 10.1063/1.4829366
<http://doi.wiley.com/10.1063/1.4829366>

To cite this version: Lalanne, Benjamin and Tanguy, Sébastien and Risso, Frédéric *Effect of rising motion on the damped shape oscillations of drops and bubbles*. (2013) *Physics of Fluids*, vol. 25 (n° 112107). pp. 1-22. ISSN 1070-6631

Any correspondence concerning this service should be sent to the repository administrator: staff-oatao@listes-diff.inp-toulouse.fr

Effect of rising motion on the damped shape oscillations of drops and bubbles

Benjamin Lalanne, Sébastien Tanguy, and Frédéric Risso

*Institut de Mécanique des Fluides de Toulouse, CNRS & Université de Toulouse,
Toulouse, France*

The objective of this work is to determine the effect of the rising motion on the dynamics of inertial shape oscillations of drops and bubbles. We have carried out axisymmetric direct numerical simulations of an ascending drop (or bubble) using a level-set method. The drop is initially elongated in the vertical direction and therefore performs shape oscillations. The analysis is based on the decomposition of the interface into spherical harmonics, the time evolutions of which are processed to obtain the frequency and the damping rate of the oscillations. As the drop accelerates, its shape flattens and oscillations no longer take place around a spherical equilibrium shape. This causes the eigenmode of oscillations to change, which results in the appearance of spherical harmonics of high order that all oscillate at the same frequency. For both drops and bubbles, the frequency, which remains controlled by the potential flow, slightly decreases with the rising velocity. The damping rate of drops, which is controlled by the dissipation within boundary layers at the interface, strongly increases with the rising velocity. At terminal velocity, the damping rate of bubbles, which results from the dissipation by the potential flow associated with the oscillating motion, remains close to that of a non-rising bubble. During the transient, the rate of deformation of the equilibrium shape of bubbles can be comparable to the oscillation frequency, which causes complex evolutions of the shape. These results extend the description of shape oscillations to common situations where gravity plays a role. In particular, the present conclusions are useful to interpret experimental results where the effect of the rising motion is often combined with that of surfactant.

I. INTRODUCTION

The size of drops (or bubbles) is a crucial feature in dispersed two-phase flows since it affects heat and mass transfers through the interfacial area, influences their motion through the drag and added-mass forces, and is of major importance in breakup and coalescence phenomena. In general, interfacial tension tends to maintain a spherical shape, whereas gravity and hydrodynamic stresses cause deformations. When the drop shape is disturbed, it may either rupture or relax toward its equilibrium shape by performing damped oscillations, which are characteristics of the proper dynamics of the interface. In an unsteady flow, the drop shape results from the coupling between the interfacial dynamics and the time-varying hydrodynamic stresses to which the interface is submitted. The knowledge of the frequencies ω_l and the damping rates β_l of the natural oscillations of the interface is therefore crucial for those who are interested to predict the breakup in unsteady flows. For a bubble immersed in a homogenous turbulence and in the absence of gravity,¹ it has been shown that the breakup rate depends on the power spectral density of the turbulent fluctuations at the frequency of the main mode of oscillation ($l = 2$) of the interface and on the damping coefficient of this mode. Later,^{2,3} the breakup probability of droplets in a strongly inhomogeneous turbulent flow has been predicted from the response of an oscillator, of parameters ω_2 and β_2 , forced by the turbulent fluctuations. A similar approach,⁴ known as Taylor Analogy Breakup (TAB), is implemented in the KIVA code and commonly used by engineers for numerical simulations of sprays. However,

the expressions of ω_l and β_l are only known for a drop oscillating around a spherical equilibrium shape.⁵⁻⁸ This constitutes a severe limitation for who has to deal with situations where the drop is subjected to a continuous deforming force since these timescales can be strongly affected by a deviation from sphericity. For instance, the oscillating frequency of a drop in a uniaxial straining flow⁹ is a decreasing function of the strength of the flow, and even vanishes when the maximal stable deformation is reached.

The motivation of the present work is to extend the knowledge of the interface dynamics to cases where drops and bubbles are free to move under the action of gravity. From a fundamental point of view, the analysis of these situations reveals the physical mechanisms coupling translational motion and shape dynamics. Moreover, it provides the basic physical parameters describing the interface response, which are required to predict deformation and breakup of drops and bubbles in unsteady configurations, such as turbulent flows.

First, let us recall the fundamentals of the dynamics of a non-spherical drop that is released in a fluid at rest in the absence of buoyancy. In the limit of small deformation, the evolution of the interface is expressed as a sum of modes,

$$r = R + \sum_{l \geq 2} \sum_{-l \leq m \leq l} a_{l,m} Y_{l,m}(\theta, \phi - \phi_{l,m}^0) \cos(\omega_l t) \exp(-\beta_l t), \quad (1)$$

where R is the radius of the non-deformed drop, $Y_{l,m}$ is the spherical harmonic of polar wavenumber l and azimuthal wavenumber m , $a_{l,m}$, and $\phi_{l,m}^0$ are the initial amplitudes and phases of mode (l,m) . The eigenfrequencies ω_l and damping rates β_l depend on l (but not on m), on the oscillating Reynolds number $Re_{osc} = \sqrt{\rho_c R \sigma} / \mu_c$, on the density ratio $\hat{\rho} = \rho_d / \rho_c$, and on the viscosity ratio $\hat{\mu} = \mu_d / \mu_c$ (where σ is the interfacial tension, ρ_c and ρ_d are the density of the continuous and dispersed phases, respectively, and μ_c and μ_d their dynamic viscosity). Note that the Ohnesorge number, $Oh = 1/Re_{osc}$, could be equivalently used. Assuming potential flow, a good approximation of the frequency is obtained:⁵

$$\omega_l^{Lamb} = \sqrt{\frac{(l-1)l(l+1)(l+2)\sigma}{(\rho_d(l+1) + \rho_c l) R^3}}. \quad (2)$$

The theoretical values of the frequencies and damping rates accounting for viscous effects, ω_l^{th} and β_l^{th} , have been determined by solving the linearized Navier-Stokes equations.⁶⁻⁸ In general, they are solutions of an implicit characteristic equation, but explicit expressions are available for large Reynolds numbers. Rigorously, ω_l^{th} and β_l^{th} correspond to the asymptotic solution that is reached after the vorticity had time to diffuse from the interface,¹⁰ but in practice they give accurate predictions even for the first period of oscillation, provided the Reynolds number is not too small.

Several theoretical,^{11,12} numerical,^{13,14} and experimental^{15,16} works considered nonlinear effects for finite deformations. They described several couplings between modes and showed an effect of the amplitude on the frequency of the oscillations. However, the statistics of the deformation and the breakup of bubbles¹ or drops^{2,3} immersed in a turbulent flow were reproduced well by computing the response of the second mode of the linear theory to the stochastic turbulent fluctuations, in situations where buoyancy plays a minor role. The linear theory thus proved to be useful to address the breakup in turbulent flows.

The major limitation of the available theory to deal with complex flows rather comes from the fact that it does not account for buoyancy and surfactants. The damping rate of the oscillations of a drop of heptane rising in water has been shown to be significantly increased because of the presence of surface-active impurities.¹⁷ Also, contrary to what is observed in microgravity conditions,¹ bubbles rising in a uniform turbulent water flow were not observed to experience surface-tension-driven oscillations after having been deformed by an intense turbulent eddy.¹⁸

The objective of this work is to characterize the oscillations of drops or bubbles made of pure fluids rising under the action of buoyancy. In this context, there exist only two theoretical results, which relate the frequency of the modes to the equilibrium shape of the interface: a calculation for a bubble rising in a liquid by means of the potential theory¹⁹ and a viscous prediction for a deformed

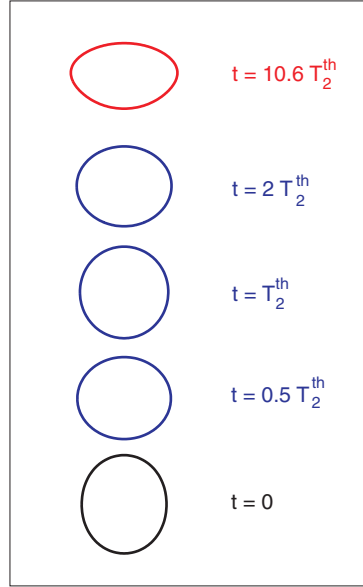


FIG. 1. Example of drop shape evolution from initial condition (black) to steady state (grey (red)) at $Re_{osc} = 100$, $Bo = 1.400$ ($Re_\infty = 270$).

bubble or drop.²⁰ As far as we know, there is no theoretical result concerning the damping rate. On the experimental side, the level of contamination of the interfaces is very hard to control, especially in liquid-liquid situations for which there is no experimental work with rising drops where the measured drag coefficient is that of a drop with clean interface. Here, the problem is addressed by means of axisymmetric numerical simulations. A drop or bubble is released in a liquid at rest. The initial shape is described by axisymmetric mode $l = 2$ with a positive amplitude and is thus approximately a prolate ellipsoid elongated in the vertical direction. A typical example of the evolution of the drop shape is given in Fig. 1. This configuration is similar to experiments in which a drop is released from a capillary.¹⁷ After the release, the drop or bubble accelerates and performs shape oscillations around an average flattened shape that evolves in time. It finally reaches a terminal velocity and a steady spheroidal oblate shape with its minor axis oriented in the vertical direction. The damped oscillations occurring during the transient stage are analyzed in order to determine which modes are involved and to measure the oscillation frequencies and damping rates.

In addition to the oscillating Reynolds number, the density ratio, and the viscosity ratio, the simulations involve two supplementary dimensionless groups: the initial deformation $a_2(t = 0)/R$ and the Bond number, $Bo = (\rho_c - \rho_d)g(2R)^2/\sigma$. Note that it can be useful to use the terminal rising Reynolds number, $Re_\infty = 2R\rho_c V_\infty/\mu_c$, instead of the Bond number, even if it is based on the bubble terminal velocity V_∞ which is not *a priori* known. Our purpose being to study the effect of the rising motion upon shape oscillations in the absence of nonlinear coupling between modes, the initial deformation is chosen small enough so that the results of the linear theory are obtained in the absence of buoyancy.

Considering what we know from the case without buoyancy, the case of a gas bubble in a liquid and that of a liquid drop in another liquid have to be distinguished. If the mode frequencies ω_l^{th} , which are controlled by a potential mechanism, are in both cases approximated well by ω_l^{Lamb} , the damping rates β_l^{th} are very different. For the bubble, the damping comes from the dissipation of the potential flow and scales as $\mu_c/\rho_c R^2$, whereas for a drop in another liquid it results from the dissipation within the boundary layers that develop on both sides of the interface and scales as $(\mu_c/\rho_c R^2)\sqrt{Re_{osc}}$. The influence of the rising motion is thus expected to be different too and we will consider the two following typical situations: ($\hat{\rho} = 0.99$, $\hat{\mu} = 1$) further referred as the *drop* case, and ($\hat{\rho} = 10^{-3}$, $\hat{\mu} = 0.016$) further referred as the *bubble* case.

Numerical simulations using level-set and ghost fluid methods have been carried out for three different oscillating Reynolds numbers ($Re_{osc} = 50, 100, 200$) and various rising Reynolds numbers Re_∞ ranging from 50 to 600 ($0.4 \leq Bo \leq 3.9$) for the *drop* case and 50 to 300 ($0.1 \leq Bo \leq 2.4$) for the *bubble* case. This corresponds to a Weber number, $We_\infty = \rho_c V_\infty^2 2R/\sigma = 1/2 (Re_\infty/Re_{osc})^2$, ranging from 3×10^{-3} to 4.

The paper is organized as follows. Section II describes the numerical code, its validation in the present context, and the post-processing. Section III presents the results of the drop case, while Sec. IV is devoted to the bubble case. Section V summarizes the main findings concerning the effect of the rising motion on the frequencies and damping rates of shape-oscillation modes.

II. NUMERICAL METHOD AND VALIDATION

A. Numerical model

Axisymmetric simulations of a rising drop (or a bubble) experiencing shape oscillations are carried out using the level-set method by means of our numerical code DIVA.^{21,22} We briefly present the outline of this method. The interface is numerically described by the zero-level curve of a continuous function ϕ , which is defined as the algebraic distance to the interface. Its displacement in a velocity field \mathbf{U} is computed by solving an advection equation:

$$\frac{\partial \phi}{\partial t} + \mathbf{U} \cdot \nabla \phi = 0.$$

The droplet motion is calculated by solving the incompressible Navier-Stokes equations by means of a projection method:

$$\frac{\partial \mathbf{U}}{\partial t} + (\mathbf{U} \cdot \nabla) \mathbf{U} + \frac{\nabla P}{\rho(\phi)} = \frac{\nabla \cdot (2\mu(\phi) \mathbf{D})}{\rho(\phi)} + \mathbf{g},$$

$$\nabla \cdot \mathbf{V} = 0,$$

where P is the pressure, μ the dynamic viscosity, ρ the density, \mathbf{g} the acceleration of the gravity, and \mathbf{D} the tensor of rate of deformation.

In these equations, ρ , μ , and P are discontinuous across the interface. The normal stress balance at the interface assumes that

$$[P]_\Gamma = \sigma \kappa + 2 \left[\mu \frac{\partial U_n}{\partial n} \right]_\Gamma,$$

where U_n is the velocity normal to the interface, n is the coordinate in the direction normal to the interface, σ the surface tension, and κ the interface curvature.

To handle the discontinuity of the pressure at the interface and calculate accurately its derivatives, a ghost fluid method has been implemented: the jump condition is extrapolated in one ghost cell on each side of the interface. The numerical formulation for the viscous term and the pressure jump at the interface follows the method detailed in Ref. 23.

An algorithm of redistancing is used to ensure that ϕ is a distance function at each time step, which needs the steady state of the following equation to be reached:

$$\frac{\partial d}{\partial \tau} = \text{sign}(\phi)(1 - |\nabla d|),$$

where $d(\mathbf{x}, t, \tau)_{\tau=0} = \phi(\mathbf{x}, t)$; τ is a fictitious time.

These partial differential equations are discretized using the finite volume technique on a staggered grid. Spatial derivatives are estimated with a second order central scheme, while a fifth order WENO scheme is used for the convective terms, which ensures that solution is robust. Temporal derivatives are approximated with a second-order Runge-Kutta scheme.

TABLE I. *Drop* case: Relative errors in the frequency and the damping rate of mode 2 for a drop that oscillates in the absence of gravity.

Number of grid points in a radius		Re_{OSC}				
		20	50	100	200	300
Frequency	16	0.42%	-0.07%	-0.51%	-0.43%	-0.60%
	32	0.26%	0.06%	0.07%	-0.27%	-0.17%
	64	0.74%	0.19%	0.01%	-0.09%	-0.11%
Damping rate	16	0.22%	0.18%	0.91%	5.67%	7.78%
	32	-1.46%	-0.68%	-0.45%	-0.07%	0.64%
	64	-2.17%	-1.15%	-1.07%	-0.76%	-0.62%

B. Validation

The numerical method has been validated on two situations: (1) the shape oscillations of drops or bubbles in the absence of gravity and (2) a weakly deformed rising bubble.

Simulations of drops and bubbles oscillating in the absence of gravity have been carried out for $20 \leq Re_{OSC} \leq 300$. The initial condition corresponds to harmonic 2 with an amplitude $a_2 = 0.075R$, which ensures to remain in the linear regime of oscillation. Tables I and II show the errors in the determination of the frequency and the damping rate by comparison with the prediction, ω_2^{th} and β_2^{th} , of the linear theory.⁸ Note that these values include both errors associated with the numerical simulation and errors in the determination of ω_2 and β_2 from the time evolution of the amplitude of harmonic 2 (see Sec. II C). Various computational grids with, respectively, 16, 32, and 64 nodes in a drop (or bubble) radius are presented. In any case, the accuracy is better for the frequency than for the damping rate because β_2 is of the second order in such a range of Reynolds numbers. A satisfactory accuracy is obtained for 32 nodes in a radius in the range of Reynolds numbers, $50 \leq Re_{OSC} \leq 200$, that will be investigated in this study.

The second validation case is based on the terminal velocity of non-oscillating rising bubbles. Tests have been done by using computational grids with 4, 8, 16, and 32 nodes in a radius. The simulations consider spherical bubbles that are released in a liquid at rest. Bond numbers smaller than 0.025 have been considered to ensure that bubbles remain almost spherical. Five rising Reynolds numbers from 20 to 100 have been investigated. For each case, the drag coefficient C_d is determined after the bubble has reached its terminal velocity. Table III presents relative errors in C_d by comparisons with predictions for spherical bubbles: Mei *et al.*²⁴ for $Re_\infty = [20, 40]$ and Moore's theory²⁵ for $Re_\infty = [60, 80, 100]$. The results show that a satisfactory accuracy is obtained from 16 nodes in a radius.

In the rest of this work, axisymmetric simulations of rising and oscillating drops or bubbles are performed on a 256×512 grid with 32 nodes in a radius. It is worth mentioning that several similar simulations have been done with the JADIM code,^{26,27} which is based on a volume of fluid method. Comparisons with the present results, which are available in Ref. 28, show a very good agreement.

TABLE II. *Bubble* case: Relative errors in the frequency and the damping rate of mode 2 for a bubble that oscillates in the absence of gravity.

Number of grid points in a radius		Re_{OSC}				
		20	50	100	200	300
Frequency	16	0.53%	-0.02%	-0.35%	-0.51%	-0.53%
	32	0.24%	-0.05%	-0.17%	-0.36%	0.41%
	64	-0.03%	-0.11%	-0.23%	-0.37%	-0.42%
Damping rate	16	1.49%	1.47%	9.75%	23.16%	41.72%
	32	-0.20%	0.32%	1.99%	7.30%	13.71%
	64	-0.31%	0.08%	0.70%	2.55%	5.36%

TABLE III. *Bubble* case: Relative error in the drag coefficient of a spherical bubble rising at terminal velocity. Reference values are given by the correlation of Mei *et al.*²⁴ for $Re_\infty = [20, 40]$ and by Moore's theory²⁵ for $Re_\infty = [60, 80, 100]$.

Re_∞	Bo	Error on C_D			
		4 nodes in R	8 nodes in R	16 nodes in R	32 nodes in R
20	0.025	+ 64.0%	- 5.0%	- 1.2%	
40	0.025	+ 129.5%	- 3.5%	- 1.6%	+2.0%
60	0.025	+ 167.5%	+2.7%	+2.1%	+5.9%
80	0.0125	+ 784.6%	+2.7%	- 3.7%	+2.7%
100	0.0125	+ 840.6%	+6.2%	- 3.7%	+2.0%

C. Post-processing of the drop shape

The drop contour in spherical coordinates, $r(\theta)$, is obtained at each time step from the zero-value line of the distance function. The successive contours are then post-processed in order to obtain parameters describing the interface dynamics: velocity $V(t)$ of the drop centre, ratio $\chi(t)$ of the horizontal to vertical maximal drop dimensions, and amplitudes $\widehat{a}_l(t)$ of spherical harmonics in the following decomposition:

$$r(\theta, t) = \widehat{a}_0 + \sum_{l=2}^{10} \widehat{a}_l(t) P_l(\cos(\theta)), \quad (3)$$

where P_l are the Legendre polynomials, \widehat{a}_0 is almost constant owing to the conservation of the drop volume since we consider only small deformations, and \widehat{a}_1 is set to zero by choosing the drop centre as origin of the coordinates. The series is stopped at $l = 10$, which is enough for an accurate description of the present drop shapes. As the drop accelerates, its equilibrium shape evolves under the action of hydrodynamic forces and the shape oscillations, which result from the initial deformation, no longer occur around a sphere, but around an oblate spheroid that flattens more and more. In order to discriminate the global evolution of the shape from the oscillations, each $\widehat{a}_l(t)$ is time-averaged over a moving window of one oscillation-period span centered on t . It is thus decomposed in a time-varying average shape $\langle \widehat{a}_l(t) \rangle$ and an oscillating component:

$$\widehat{a}_l(t) = \langle \widehat{a}_l(t) \rangle + a_l(t). \quad (4)$$

The same decomposition is carried out for the aspect ratio $\chi(t)$.

Examples of time evolutions of the drop parameters are shown in Fig. 2 for case ($Re_{OSC} = 100$, $Bo = 1.400$, $Re_\infty = 270$) with various initial amplitudes of deformation. Note that time is normalized by the period, $T_2^{th} = 2\pi/\omega_2^{th}$, of mode 2 in the absence of gravity.

Figures 2(a) and 2(b) present the decomposition of harmonic 2. Figure 2(c) shows the instantaneous rising Reynolds number, $Re_{ASC} = 2R\rho_c V(t)/\mu_c$. Figure 2(d) is a semi-log plot of the local maxima of $|a_2(t)|$ that are reached at instants t_i . A careful examination of Fig. 2(b) reveals that the frequency ω_2 of the oscillations is not constant. Moreover, Fig. 2(d) shows that the values of $\log(|a_2(t_i)|)$ do not lay on a straight line, which means that the damping coefficient β_2 is also a function of time. In the following, the frequency and the damping rate will be determined at each instant corresponding to a local extremum of $a_2(t)$: $\omega_2(t_i) = 2\pi/(t_{i+1} - t_{i-1})$ and $\beta_2(t_i) = [\log(|a_2(t_{i-1})|) - \log(|a_2(t_{i+1})|)]/(t_{i+1} - t_{i-1})$. (Note that the results at $t_0 = 0$ and t_1 are discarded to remove edge effects resulting from the time-averaging procedure.)

D. Linearity of the oscillations

The objective of this work is to determine the effect of the rising motion on the drop shape oscillations in the linear regime. The smaller the deformation, the smaller nonlinear effects. But, the larger the deformation, the more accurate the description of the oscillations. We have therefore to choose the largest initial deformation that allows results independent of it.

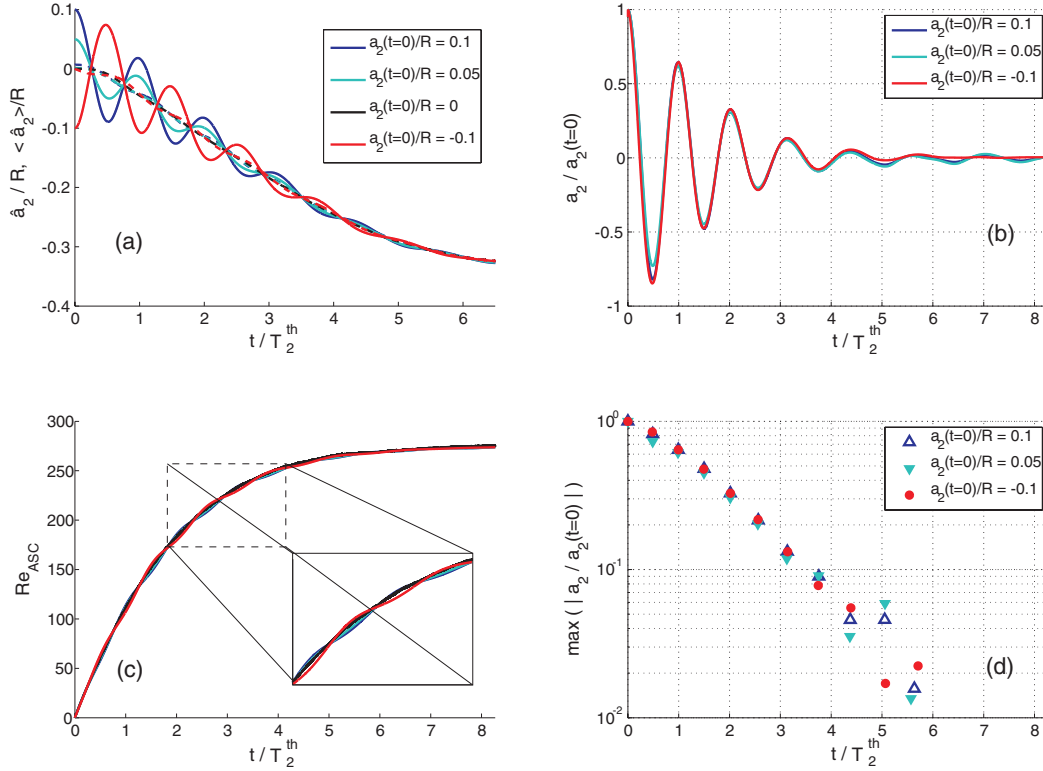


FIG. 2. Time evolution of a rising drop at $Re_{OSC} = 100$ and $Bo = 1.400$ ($Re_\infty = 270$) for different initial amplitudes $a_2(t=0)/R = \{-0.10, 0, 0.05, 0.10\}$. (a) Harmonic \hat{a}_2 [—] and its time-varying average $\langle \hat{a}_2 \rangle$ [- - -]. (b) Oscillating component a_2 obtained by subtraction of $\langle \hat{a}_2 \rangle$. (c) Instantaneous rising Reynolds number Re_{ASC} . (d) Maxima and minima of $a_2(t)/a_2(t=0)$.

Figure 2 compares results obtained for $a_2(t=0)/R = \{-0.10, 0, 0.05, 0.10\}$. Figure 2(a) shows that the average deformation of cases with either an initial prolate ($a_2(t=0)/R = 0.05$ or 0.10) or oblate ($a_2(t=0)/R = -0.10$) shape is similar to that of the case with an initial spherical shape ($a_2(t=0) = 0$). Moreover, all cases with non-zero initial deformation show similar evolutions of harmonic 2 (Fig. 2(b)) and of rising velocity (Fig. 2(c)) up to $t = 4.5 T_2^{th}$. For larger times, a_2 becomes lower than $1/5$ of the mesh-grid spacing ($\approx 0.005R$), which does not allow an accurate determination of its local extrema (Fig. 2(d)). The frequency and the damping have been computed while a_2 is larger than this threshold.

For all the cases considered above, the oscillations clearly belong to the linear regime. For the rest of this study, the initial amplitude is set to $a_2(t=0)/R = 0.10$ for drops and $a_2(t=0)/R = 0.075$ for bubbles.

III. RESULTS FOR A LIQUID DROP IMMERSSED IN ANOTHER LIQUID

The drop case corresponds to both density and viscosity ratios close to unity ($\hat{\rho} = 0.99$, $\hat{\mu} = 1$). Three Reynolds numbers of oscillation ($Re_{OSC} = 50, 100$, and 200) and various Bond numbers ($0.4 \leq Bo_\infty \leq 3.9$) have been investigated, corresponding to rising Reynolds numbers in the range $50 \leq Re_\infty \leq 600$ (Table IV).

A. Velocity, mean shape, and modes of oscillation

Time evolutions of the drop velocity, Re_{ASC} , and the aspect ratio, χ , are reported in Fig. 3 for all investigated cases. The initial condition corresponds to a drop at rest ($Re_{ASC} = 0$), the shape of which is elongated in the vertical direction ($\chi < 1$). As the drop accelerates, χ globally increases

TABLE IV. Drops: Parameters of the simulations (Re_{OSC} and Bo), corresponding to the cases of Fig. 3. The Reynolds number of rising and the aspect ratio of the terminal shape are given when the terminal velocity can be considered as reached in the simulations.

Reference on Fig. 3	Parameters		Results	
	Re_{OSC}	Bo	Re_{∞}	χ_{∞}
1	50	0.430		
2	50	0.640	68	1.08
3	50	1.100	99	1.19
4	50	1.725	129	1.47
5	50	2.480	145	1.82
6	50	3.880		... ^a
7	100	0.430		
8	100	0.970		
9	100	1.400	270	1.68
10	100	1.725	287	1.93
11	100	2.700		... ^a
12	200	0.670		
13	200	0.970	542	1.79
14	200	1.320		... ^a

^aSelf-sustained oscillations are present.

and experiences oscillations. Concurrently, the velocity shows only slight oscillations, indicating a very weak influence of shape oscillations upon the drop velocity. At the highest rising Reynolds numbers, self-sustained oscillations of both shape and velocity are observed. These oscillations are not characteristic of the proper dynamics of the interface since they are forced by hydrodynamic instabilities that develop within the drop wake. Moreover, even though imposing the axial symmetry is relevant when the axisymmetric solution is stable, it is unphysical when describing such a path instability. Therefore, we will stop considering the results as soon as these self-sustained oscillations appear. We are confident concerning the results in the stable case because they have been proved to be independent of the mesh spacing and validated by comparison with another code.

Figure 4 shows the instantaneous average aspect ratio $\langle\chi(t)\rangle$ as a function of the instantaneous Weber number $We(t) = \rho_c V^2(t)2R/\sigma$, for all simulated drops. The results nicely gather close to a master curve, which is linear up to $We(t) \approx 1.5$ and $\langle\chi(t)\rangle \approx 1.15$. As expected in this range of rising Reynolds numbers, this confirms that inertia associated to the translational motion is responsible for the average drop deformation.

The aspect ratio gives a global information about the shape. A more detailed description is obtained from the decomposition into spherical harmonics, as illustrated in Fig. 5 where the time evolutions of harmonics 2, 3, and 4 are plotted for one of the largest Weber number investigated: $We_{\infty} = 3.0$ for $Re_{OSC} = 100$ and $Bo = 0.970$. Consider first the average drop shape (dashed lines in Fig. 5(a)). The magnitude of all harmonics starts from zero (spherical shape) and then regularly increases up to the terminal shape. Harmonic 2 is clearly dominant and takes negative values since the drop is flattened. Harmonic 3, which accounts for the fore-aft asymmetry, is weak and negative: $\langle\hat{a}_3\rangle \approx 0.1 \langle\hat{a}_2\rangle$ at terminal velocity for all considered Weber numbers. Harmonic 4 is moderate and positive, but its magnitude relative to that of harmonic 2 increases with the Weber number to reach $\langle\hat{a}_4\rangle \approx 0.3 |\langle\hat{a}_2\rangle|$ for $We_{\infty} = 3.5$, indicating that the shape becomes more complex as the Weber number increases.

We consider now the oscillations. Figure 5(b) shows the time evolution of spherical harmonics. Owing to the chosen initial condition, harmonic 2 is dominant all along the simulation. However, harmonics 3 and 4, which are absent at the start of the simulation, are generated during the first period of oscillations. Then, from the second period, a_2 , a_3 , and a_4 are observed (1) to oscillate at the same frequency, (2) to decay at the same rate, and (3) to have constant phases relative to each other. Because we have taken care to operate in the linear regime, the existence of higher harmonics is not the consequence of nonlinear interactions between modes. The reason is that the eigenmodes

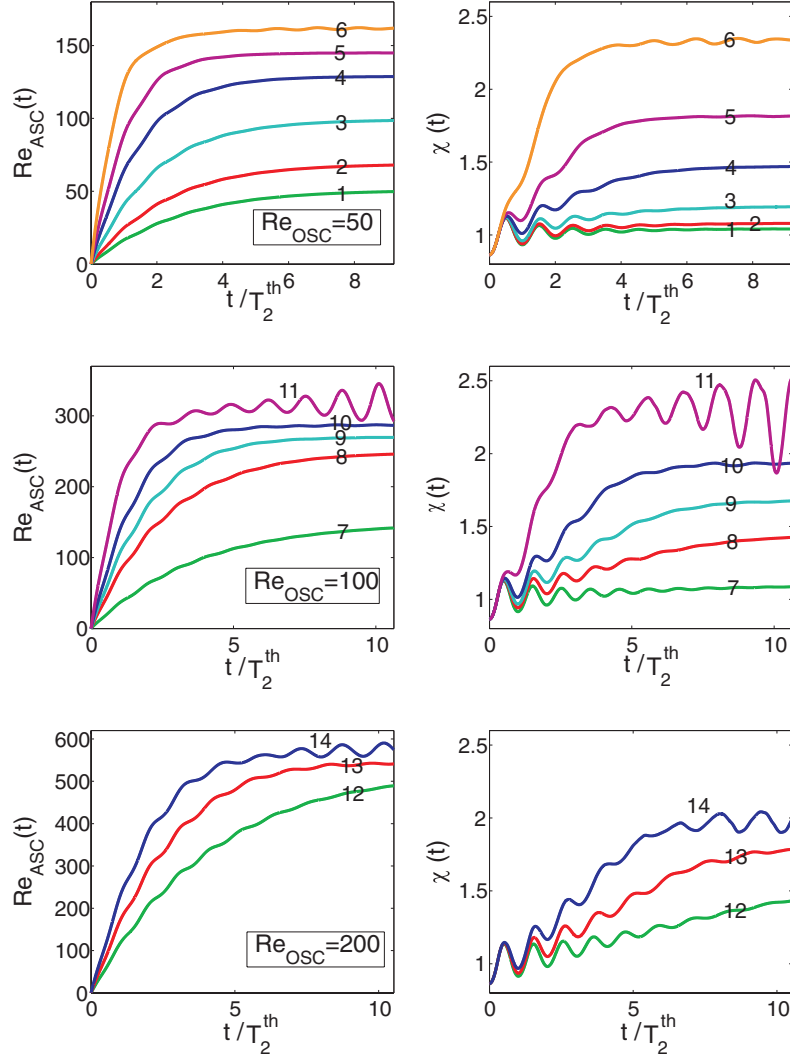


FIG. 3. Drops: Time evolutions of the rising Reynolds number, Re_{ASC} , and the aspect ratio, χ , for $Re_{OSC} = \{50, 100, 200\}$ and various Bo . The parameters of each case are given using the numerical labels in Table IV.

of shape oscillations are modified as the average shape varies. Whereas spherical harmonics are the eigenvectors of the oscillations around a spherical equilibrium shape, the eigenvectors of the oscillations around an equilibrium shape that involves several spherical harmonics ($\langle \hat{a}_2 \rangle$, $\langle \hat{a}_3 \rangle$, $\langle \hat{a}_4 \rangle$) involves itself several spherical harmonics (a_2 , a_3 , a_4).¹⁹ The fact that a single frequency, a single damping rate and a single phase are observed after the initial transitory stage suggests that a single mode is present. Following Meiron,¹⁹ we will label it *mode 2* by continuity with the corresponding eigenmode at $We = 0$. Expressed in this new basis, shape oscillations involve this single mode. Nevertheless, this new basis is not suitable to describe the equilibrium shape.

Since harmonic 2 is predominant during the initial stage of the simulation and sufficient to characterize the eigenmode that controls the final stage, it is relevant to focus on its frequency and damping rate.

B. Frequency and damping rate

Figure 6 shows examples of time evolutions of ω_2 and β_2 for $Re_{OSC} = 100$ and various Bo . At $t = 0$, both frequency and damping rate are equal to the theoretical values in the absence of

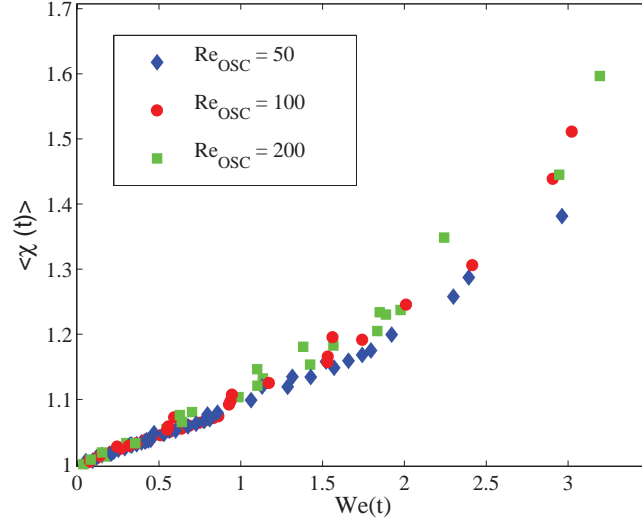


FIG. 4. Drops: Aspect ratio of the average shape $\langle \chi(t) \rangle$ against the instantaneous Weber number $We(t)$ for all investigated cases.

gravity. Then, as the drop accelerates, the frequency slightly decreases (-16% at $Bo = 1.725$), whereas the damping rate strongly increases ($+230\%$ at $Bo = 1.725$). The larger the rising velocity, the larger the deviations. This suggests investigating whether there exists a simple relation between these deviations and the instantaneous velocity. In Fig. 7(a) (respectively, 7(b)), the values of ω_2/ω_2^{th} (respectively, β_2/β_2^{th}) for all cases and instants are plotted against the instantaneous Weber number, $We(t)$, which is proportional to the square of the ratio of the rising velocity to the oscillating velocity: $Re_{ASC}(t)/Re_{OSC} \sim V(t)/R\omega_2^{th}$. Thereby, both frequency and damping rates are gathered around a master curve. Even though a certain scattering indicates that other factors – such as Bond number, drop acceleration, or motion history – also play a role, the deviations are mainly controlled by the instantaneous velocity. It is worth mentioning that at small deformation, the present results show a deviation in the frequency of oscillation as $\omega_2/\omega_2^{th} = 1 + \langle a_2 \rangle / R$, whereas the theory of Subramanyam²⁰ predicts a much weaker deviation as $\omega_2/\omega_2^{th} = 1 + 1/8 \langle a_2 \rangle / R$. This theory is clearly not able to tackle the complexity of this problem.

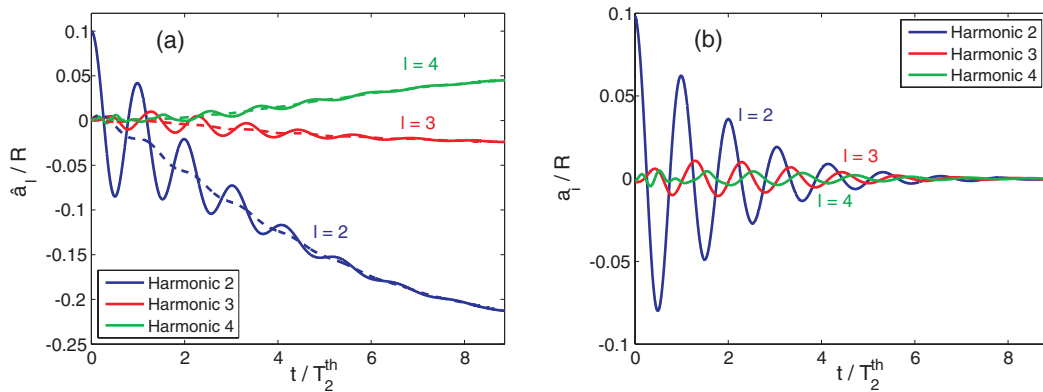


FIG. 5. Drops: Decomposition in spherical harmonics for case $Re_{OSC} = 100$ and $Bo = 0.970$ ($Re_\infty = 246$, $We_\infty = 3.0$). (a) Total amplitude \hat{a}_l and average deformation $\langle \hat{a}_l \rangle$. (b) Amplitude a_l of the oscillations around the average shape.

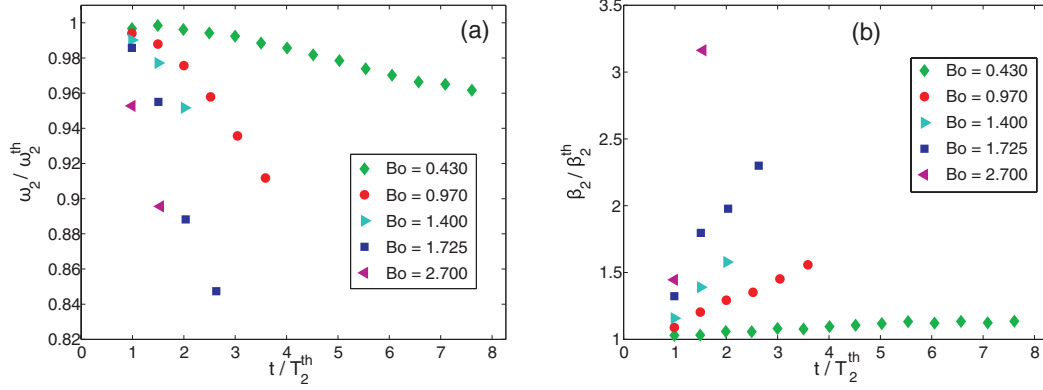


FIG. 6. Drops: Time evolution of oscillation properties for $Re_{OSC} = 100$ and various Bo . (a) Normalized frequency ω_2/ω_2^{th} . (b) Normalized damping rate β_2/β_2^{th} .

C. Discussion of mechanisms

The rising motion has a strong impact on the damping rate, whereas it slightly alters the frequency. This difference in behavior can be explained by a difference of physical mechanism. The frequency is controlled by the potential flow associated with the oscillatory deformation of the interface. Deviations in the frequency are caused by the evolution of the eigenmode as equilibrium shape changes. On the other hand, the dissipation is controlled by the vorticity generation within the boundary layers that develop at the interface as the interface oscillates: at $Re_{OSC} = 100$, the contribution of the term proportional to the square root of the oscillating Reynolds number represents 90% of the damping rate for a drop in the absence of gravity.

More insight in the mechanism responsible for the damping can be gained from the examination of the vorticity field. Let us compare the five cases defined in Table V, which correspond to the same oscillating Reynolds number and are considered at an instant where the amplitude of the shape oscillation is minimum and the associated kinetic energy is maximum: $D_{S_{OSC}}$, a drop oscillating in the absence of gravity; $D_{S_{noOSC}}$, a drop that rises slowly with a damping rate close to the value in the absence of gravity; $D_{F_{OSC}}$, a drop that rises rapidly and shows a strong deviation in the damping rate (fast drop); $D_{S_{noOSC}}$ and $D_{F_{noOSC}}$, the same cases as $D_{S_{OSC}}$ and $D_{F_{OSC}}$ but without initial deformation, so with negligible shape oscillations.

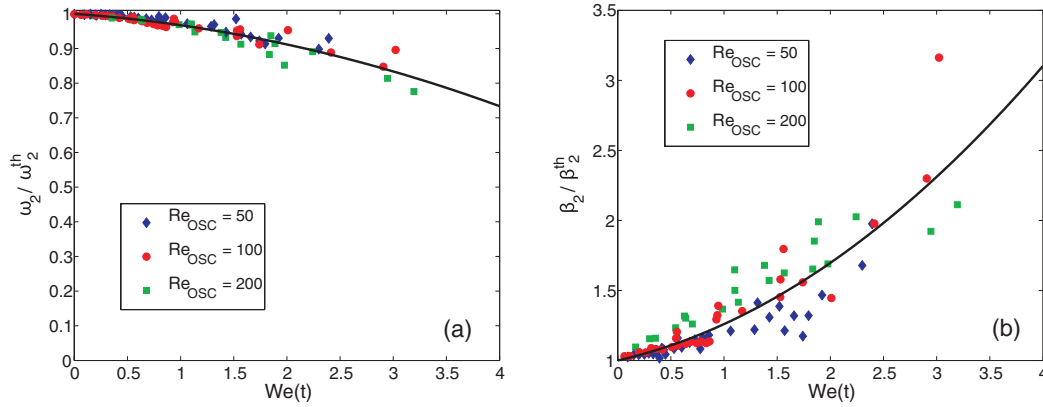


FIG. 7. Drops: (a) Normalized frequency and (b) damping rate against the instantaneous Weber number for all considered cases and instants. Continuous lines [—]: Fitting curves $\omega_2/\omega_2^{th} = -0.0112 We^2(t) - 0.0218 We(t) + 1.00$ and $\beta_2/\beta_2^{th} = 0.0887 We^2(t) + 0.1710 We(t) + 1.00$.

TABLE V. Drops: Parameters of the selected cases for examination of vorticity fields at $t^* = (3 + 1/4)T_2^{th}$.

Drop	Re_{OSC}	Bo	$a_2(t=0)/R$	Re_∞	$Re_{ASC}(t^*)$	$We(t^*)$	$\omega_2(t^*)/\omega_2^{th}$	$\beta_2(t^*)/\beta_2^{th}$	$\langle \chi(t^*) \rangle$
D_{0OSC}	100	0.000	0.10	0	0	0.00	1.0	1.0	1.0
D_{SOSC}	100	0.105	0.10	50	23	0.02	1.0	1.0	1.0
D_{SnoOSC}	100	0.105	0.00	50	23	0.02			1.0
D_{FOOSC}	100	1.725	0.10	287	264	3.5	0.8	2.3	1.6
D_{FnoOSC}	100	1.725	0.00	287	264	3.5			1.6

Figure 8(a) shows the vorticity field of the non-rising drop D_{0OSC} , while Fig. 8(b) shows that of the slow-rising oscillating drop D_{SOSC} . The two vorticity fields have a very different structure. The vorticity of the non-rising case is anti-symmetric about the drop equator and takes a negative extremum value at $\theta = \pi/4$ and a positive one at $\theta = 3\pi/4$, which are the locations of the nodes of the shape oscillation where the tangential fluid velocity is maximum. By contrast, the vorticity of the rising oscillating case keeps the same sign all over the flow field and shows a single maximum. Moreover, the magnitude of the vorticity of the rising case is more than twice that of the non-rising case. Figure 9(a) shows the vorticity of the slow-rising non-oscillating case D_{SnoOSC} . Its structure and magnitude are similar to that of rising oscillating case, which means that the production of vorticity by the translational motion dominates that by the oscillating motion, even though the rising velocity remains moderate and the wake has not yet achieved its development. Figure 9(b) presents the subtraction of the vorticity field of the slowly rising case without oscillation (D_{SnoOSC} , Fig. 9(a)) from that of the slowly rising case with oscillation (D_{SOSC} , Fig. 8(b)). The result is very similar to that of the non-rising case (D_{0OSC} , Fig. 8(a)), which leads to the conclusion that the vorticity generated by the oscillatory motion and the vorticity generated by the rising motion do not influence each other. For a slowly rising bubble, the damping rate remains the same as that of a non-rising drop, even though the vorticity generated by the translation is larger than the vorticity produced by the shape oscillation.

Figure 10(a) shows the vorticity field corresponding to the rapidly rising and oscillating case D_{FOOSC} . At the considered instant, the drop has almost reached its terminal velocity and a developed wake is present. The maximum vorticity is 70 times larger than that of the non-rising case D_{0OSC} . Figure 10(b) shows the subtraction of the vorticity field of the rapidly rising case without oscillation (D_{FnoOSC} , not presented) from that of the rapidly rising case with oscillation (D_{FOOSC} , Fig. 10(a)). Contrary to what observed in the slowly rising case (Fig. 9(b)), Fig. 10(b) is totally different from the non-rising case (Fig. 8(a)). When the rising motion is fast, the vorticity associated to the

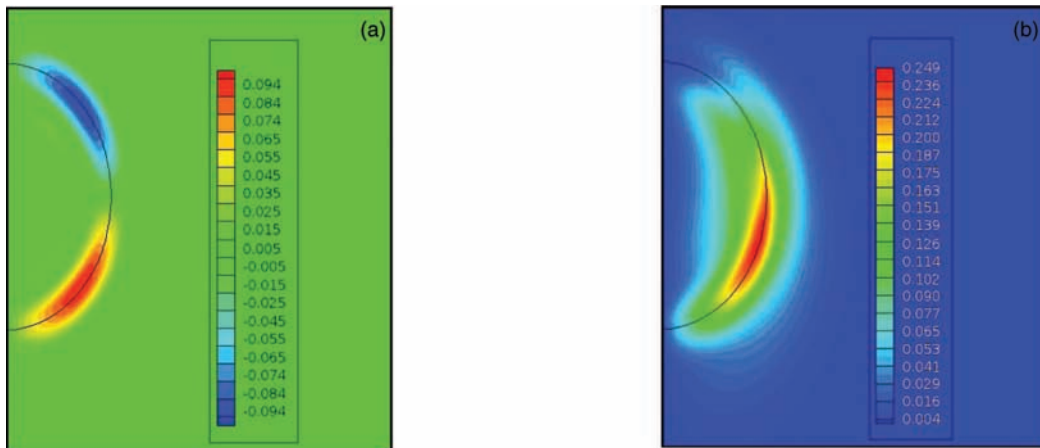


FIG. 8. Drops: (a) Vorticity field for a non-rising oscillating drop (D_{0OSC}), normalized by ω_2^{th} . (b) Vorticity field for a slowly rising oscillating drop (D_{SOSC}), normalized by ω_2^{th} .

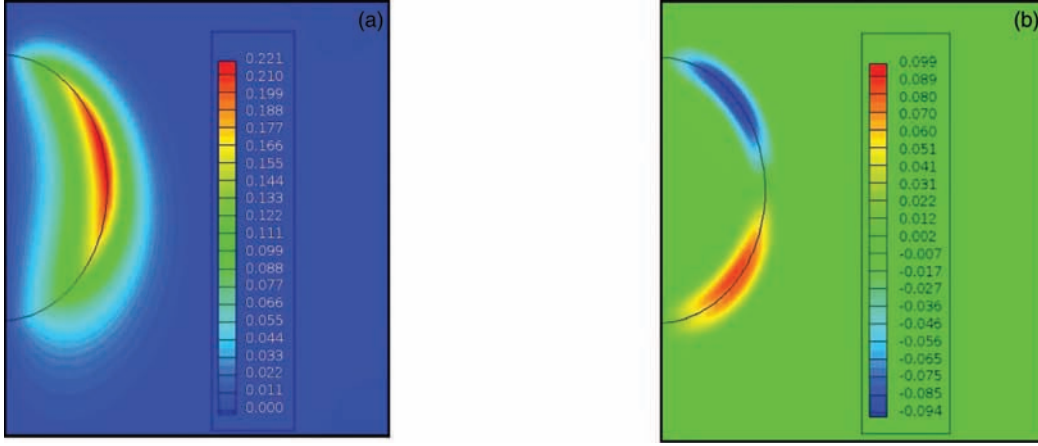


FIG. 9. Drops: (a) Vorticity field for a slowly rising non-oscillating drop ($D_{S_{no OSC}}$), normalized by ω_2^{th} . (b) Vorticity field of the slowly rising oscillating drop ($D_{S_{OSC}}$, Fig. 8(b)) minus that of the slowly rising non-oscillating drop ($D_{S_{no OSC}}$, Fig. 9(a)), normalized by ω_2^{th} .

oscillatory motion is no longer independent of the vorticity associated to the translational motion; the corresponding boundary layers interact, leading to an increase of the damping rate of the shape oscillations.

IV. RESULTS FOR A GAS BUBBLE IMMERSSED IN A LIQUID

For the bubble case, density and viscosity ratios correspond to those of air in water ($\hat{\rho} = 0.001$, $\hat{\mu} = 0.016$). Three Reynolds numbers of oscillation ($Re_{OSC} = 50, 100, \text{ and } 200$) and various Bond numbers ($0.1 \leq Bo_\infty \leq 2.4$) have been investigated, corresponding to rising Reynolds numbers in the range $50 \leq Re_\infty \leq 300$ (Table VI).

A. Velocity, mean shape, and oscillations

Time evolutions of the bubble velocity, Re_{ASC} , and the aspect ratio, χ , are reported in Fig. 11 for all investigated cases. The initial condition is similar to that of drops: bubble at rest ($Re_{ASC} = 0$) and

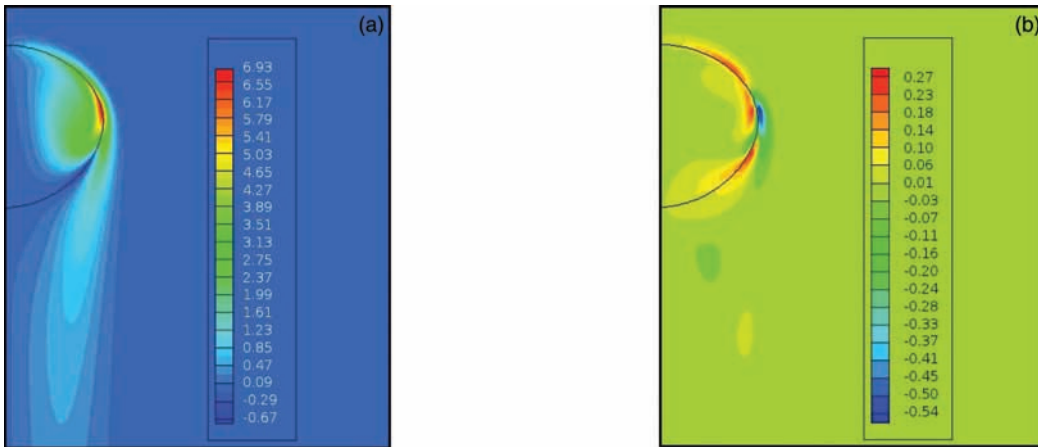


FIG. 10. Drops: (a) Vorticity field for a rapidly rising and oscillating drop ($D_{F_{OSC}}$), normalized by ω_2^{th} . (b) Vorticity field of the rapidly rising and oscillating drop ($D_{F_{OSC}}$, Fig. 10(a)) minus that of the rapidly rising but non-oscillating drop ($D_{F_{no OSC}}$), normalized by ω_2^{th} .

TABLE VI. Bubbles: Parameters of the simulations (Re_{OSC} and Bo), corresponding to the cases of Fig. 11. The Reynolds number of rising and the aspect ratio of the terminal shape are given when the terminal velocity has been reached before the end of the simulations. Please note that case 9 appears twice in Fig. 11: once with $a_2(t=0)/R = 0.075$, once with $a_2(t=0)/R = -0.075$.

Reference on Fig. 11	Parameters		Results	
	Re_{OSC}	Bo	Re_∞	χ_∞
1	50	0.260		
2	50	0.670	89	1.23
3	50	1.050	110	1.41
4	50	1.510	127	1.66
5	50	2.360	144	1.99
6	100	0.066	49	1.01
7	100	0.380		
8	100	0.590		
9	100	1.050	257	1.81
10	100	1.270		
11	100	1.640		
12	200	0.066		
13	200	0.260		
14	200	0.590		

elongated in the vertical direction ($\chi < 1$). By contrast with drops, the rising velocity V of bubbles experiences oscillations of significant amplitudes at the same frequency as shape oscillations. Its time evolution has been computed by using the balance between the added-mass, drag, and buoyancy forces that act on a spheroidal bubble (under the assumption $\rho_d \ll \rho_c$):

$$\rho_c \frac{4}{3} \pi R^3 \frac{d C_M V}{dt} = -C_D \frac{\pi R^2}{2} \rho_c V^2 - \rho_c \frac{4}{3} \pi R^3 g. \quad (5)$$

At each instant, the added-mass coefficient is given by $C_M = \frac{\beta_0}{2 - \beta_0}$, with $\beta_0 = (\zeta^2 + 1)\zeta \cot^{-1} \zeta - \zeta^2$ and $\zeta = (\chi^2 - 1)^{-1/2}$, where χ is the instantaneous aspect ratio issued from the direct numerical simulation. For the drag coefficient, we use the expression given by Moore²⁹ which is valid in this range of rising Reynolds number and aspect ratio: $C_D = \frac{48}{Re_{ASC}} G(\chi) \left[1 + \frac{H(\chi)}{Re_{ASC}^{1/2}} \right]$, where $G(\chi)$ and $H(\chi)$ are two functions of the aspect ratio. Dotted lines in Fig. 11 show the time evolutions of Re_{ASC} obtained by solving Eq. (5) for the case $Re_{OSC} = 100$. The agreement between this elementary force balance and the direct numerical simulation is very good. It is worth noting that using the instantaneous aspect ratio, $\chi(t)$, or the average one, $\langle \chi(t) \rangle$, has negligible influence on the computed rising velocity. We can therefore conclude that the coupling between shape oscillations and rising velocity results from the variations of the added-mass coefficient, as previously stated by de Vries *et al.*:³⁰ as the bubble stretches, the added-mass coefficient decreases and the bubble acceleration increases; as the bubble flattens, the added-mass coefficient increases and the bubble acceleration decreases. As a consequence, even though there are periods during which the bubble does not accelerate, the kinetic energy of the liquid that is entrained in the bubble rising motion regularly increases.

Figure 12 shows the instantaneous average aspect ratio $\langle \chi(t) \rangle$ as a function of the instantaneous Weber number $We(t)$, for all simulated bubbles. Similarly to drops, the results nicely gather around a master curve, confirming the predominant role of inertia associated to the translational motion in the determination of the average shape. The present results match the prediction of the potential theory by Benjamin³¹ (plain line) only for small deformations ($\langle \chi(t) \rangle < 1.1$), whereas they are in good agreement with the experimental correlation (dotted line) by Legendre *et al.*³² in the whole range of considered We .

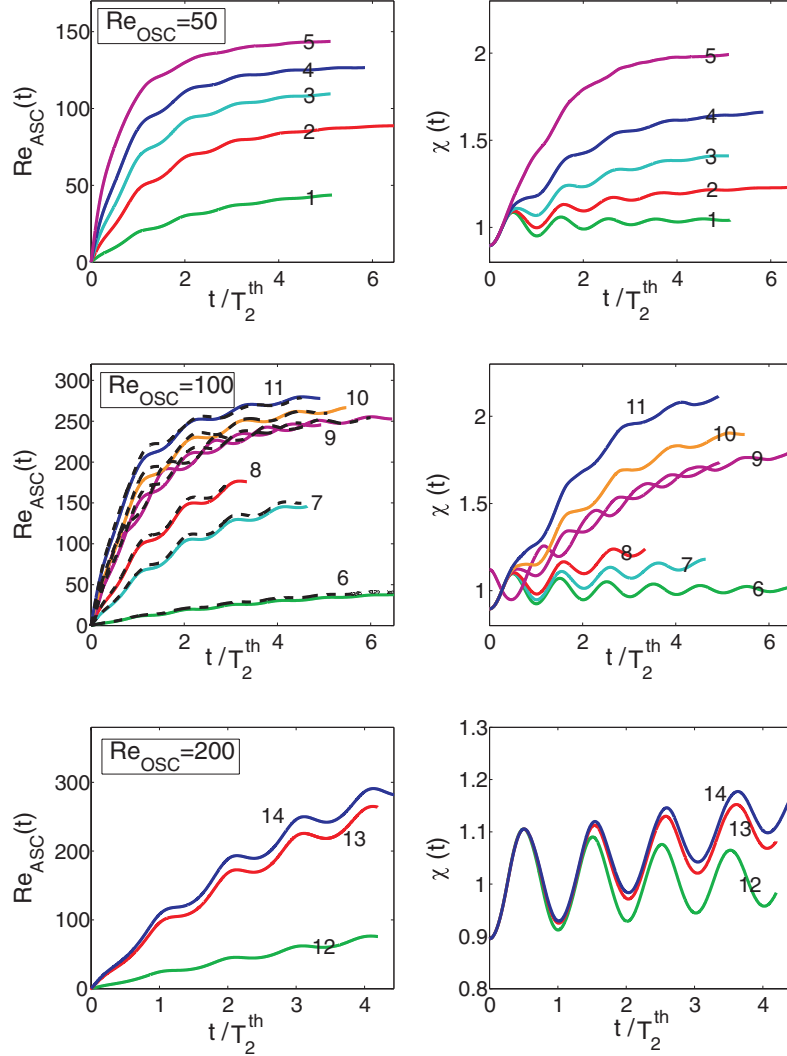


FIG. 11. Bubbles: Time evolutions of the rising Reynolds number, Re_{ASC} , and the aspect ratio, χ , for $Re_{OSC} = \{50, 100, 200\}$ and various Bo . The parameters of each case are given using the numerical labels in Table VI.

The time evolutions of spherical harmonics 2, 3, and 4 are presented in Fig. 13 for a representative case at $We_\infty \approx 3.6$, for $Re_{OSC} = 100$ and $Bo = 1.270$. The average bubble shape is shown by dashed lines in Fig. 13(a). Its evolution follows similar trends as in the drop case: $\langle \hat{a}_2 \rangle$ is negative and its magnitude increases; $\langle \hat{a}_3 \rangle$ is weak and negative; $\langle \hat{a}_4 \rangle$ increases by taking moderate positive values. Also, the ratios $\langle \hat{a}_3 \rangle / \langle \hat{a}_2 \rangle$ and $\langle \hat{a}_4 \rangle / \langle \hat{a}_2 \rangle$ at terminal velocity are similar for drops and bubbles. However, for same We_∞ and Re_∞ , larger values of $|\langle \hat{a}_2 \rangle|$ are reached for bubbles than for drops. Bubbles and drops therefore take the same average shapes, but the maximal deformation and the rate of deformation of bubbles are larger.

We consider now the oscillations around the average shape. At small Weber number, harmonic 2 remains dominant all along the simulation: a_3 and a_4 are more than 5 times smaller than a_2 for $We_\infty \leq 0.7$. At larger We , the time evolutions of the harmonics show two stages, as illustrated in Fig. 13(b) for $We_\infty \approx 3.6$. Until $t = 1.5 T_2^{th}$, harmonic 2 decreases fast while higher harmonics grow. After this initial stage, the amplitudes of harmonics 2, 3, and 4 are of the same order of magnitude and no longer evolve relative to each other. As observed for drops, all harmonics oscillate at the same frequency – close to ω_2^{th} – and with the same damping rate. For the same reasons, we conclude that a single eigenmode is present, which will again be labelled *mode 2* by continuity with

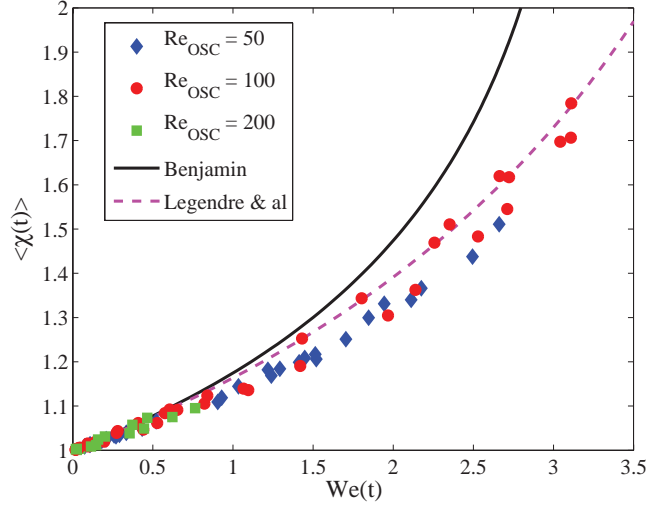


FIG. 12. Bubbles: Aspect ratio of the average shape $\langle \chi(t) \rangle$ against the instantaneous Weber number $We(t)$ for all investigated cases. Comparisons with the relations by Benjamin³¹ and Legendre *et al.*³²

the corresponding eigenmode of the oscillations around a spherical shape. A major difference with drops is that its decomposition brings into play the different harmonics with significant amplitudes.

Another capital difference will be revealed by the examination of the frequency and the damping rate. Prior to discussing their time evolution in Sec. IV B, an important conclusion should be drawn from the previous analysis. The frequency ω_2 of harmonic 2 is representative of shape oscillations during the whole simulation, whereas its damping rate β_2 is sufficient to characterize the evolution of the energy of shape oscillations only during the final stage when a single mode is present. During the transitory stage where higher harmonics are growing, β_2 is not representative of the evolution of the total energy of oscillations.

B. Frequency and damping rate

Figure 14 shows examples of time evolutions of ω_2 and β_2 for $Re_{OSC} = 100$ and various Bo . Evolutions of β_3 and β_4 are also plotted for case $Bo = 1.05$ ($Re_\infty = 257$). Frequency and damping rate are again functions of time.

Concerning frequency (Fig. 14(a)), trends are similar to drops. The frequency decreases as the drop accelerates: the larger the velocity, the larger the deviation with respect to the theoretical

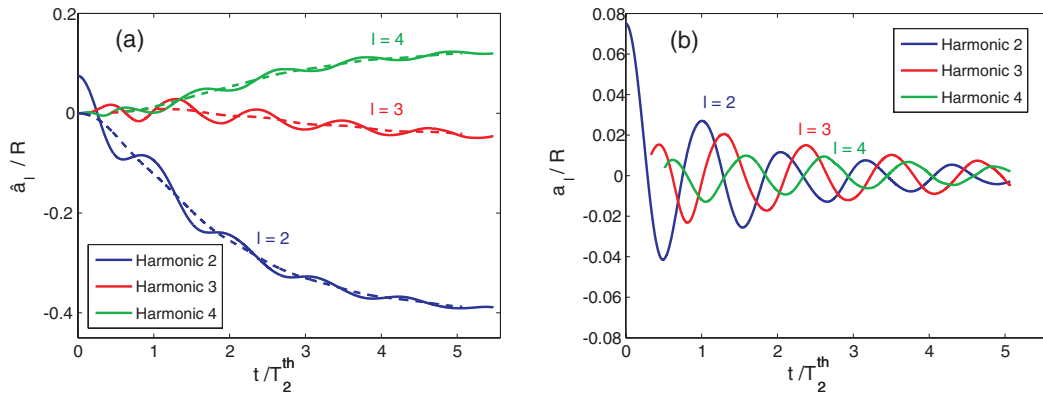


FIG. 13. Bubbles: Decomposition in spherical harmonics for cases $Re_{OSC} = 100$ and $Bo = 1.270$ ($Re_\infty \approx 270$, $We_\infty \approx 3.6$). (a) Total amplitude \hat{a}_l and average deformation $\langle \hat{a}_l \rangle$. (b) Amplitude a_l of the oscillations around the average shape.

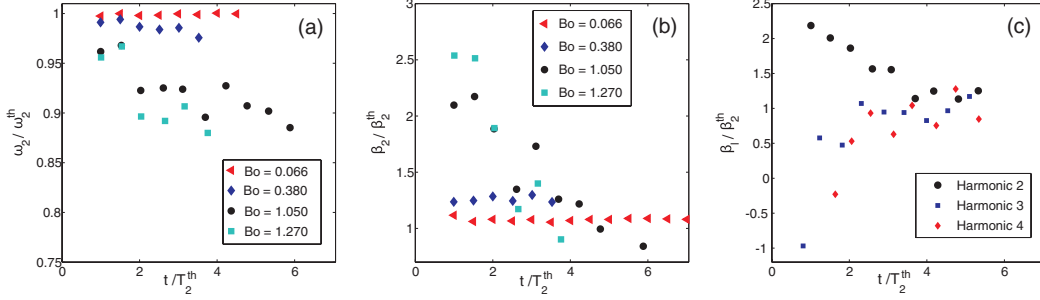


FIG. 14. Bubbles: Time evolution of oscillation properties for $Re_{OSC} = 100$ and various Bo . (a) Normalized frequency ω_2/ω_2^{th} . (b) Normalized damping rate β_2/β_2^{th} . (c) Normalized damping rates β_2/β_2^{th} , β_3/β_2^{th} , β_4/β_2^{th} for case $Bo = 1.050$ ($Re_\infty = 257$, $We_\infty = 3.3$).

value in the absence of gravity. However, the effect remains moderate since the maximum observed deviation is less than 15%. In Fig. 15(a), the values of $\omega_2(t)/\omega_2^{th}$ for all cases and instants are plotted against the average aspect ratio $\langle\chi\rangle(t)$. The results gather around the potential prediction of Meiron,¹⁹ who calculated the eigenmodes of a non-spherical bubble that rises at terminal velocity (Note that a similar collapse of the results is obtained by plotting $\omega_2(t)/\omega_2^{th}$ against $We(t)$). Despite the residual scattering that is probably due to the fact that the bubbles are accelerating fast, the good agreement with Meiron's theory indicates that observed frequency deviations correspond to the evolution of the eigenmodes of oscillations as the bubble shape changes.

Concerning damping rate, behaviour of bubbles is totally different from drops. At low Bond number, β_2/β_2^{th} remains close to unity during the entire simulation, whereas at large Bo , it presents a high value at the beginning of the acceleration stage and then decreases towards unity as the bubble approaches its terminal velocity (Fig. 14(b)). Consistent trends are observed for β_3/β_2^{th} and β_4/β_2^{th} : at low Bo , a_3 and a_4 remain close to zero, whereas at large Bo , β_3/β_2^{th} and β_4/β_2^{th} start from a strong negative value to tend towards unity (Fig. 14(c)). The instantaneous values of β_2 , β_3 , and β_4 are clearly not correlated to the instantaneous bubble velocity. These results can be understood by considering the evolution of the average bubble shape from the initial state until the final stage when the bubble rises at constant velocity. At $t = 0$, the bubble is at rest and its equilibrium shape is spherical: shape oscillations are thus characterized by a frequency ω_2^{th} , a damping rate β_2^{th} , and eigenvectors that are the spherical harmonics. As the bubble accelerates, the bubble flattens more and more and the eigenmodes of oscillation have to continuously adapt to the evolving equilibrium

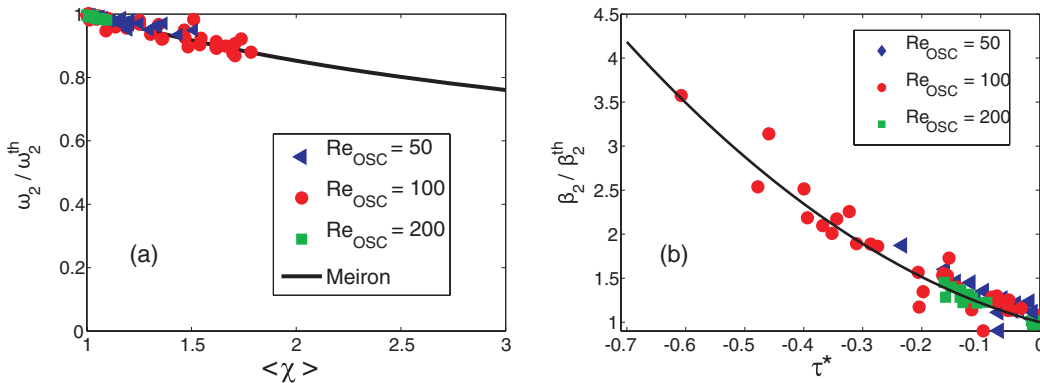


FIG. 15. Bubbles: Parameters of bubble oscillations for all considered cases and instants. (a) $\omega_2(t)/\omega_2^{th}$ against the instantaneous average aspect ratio $\langle\chi\rangle(t)$. [—] Fitting of Meiron's result:¹⁹ $\omega/\omega^{th} = 0.0006\langle\chi\rangle^4 - 0.0102\langle\chi\rangle^3 + 0.0745\langle\chi\rangle^2 - 0.3077\langle\chi\rangle + 1.2428$. (b) $\beta_2(t)/\beta_2^{th}$ against the normalized rate of change of the average shape: $\tau^* = \frac{1}{R\beta_2^{th}} \frac{d\langle a_2 \rangle}{dt}$. [—] Fitting curve: $\beta_2/\beta_2^{th} = 3.9605\tau^{*2} - 1.7770\tau^* + 1.00$.

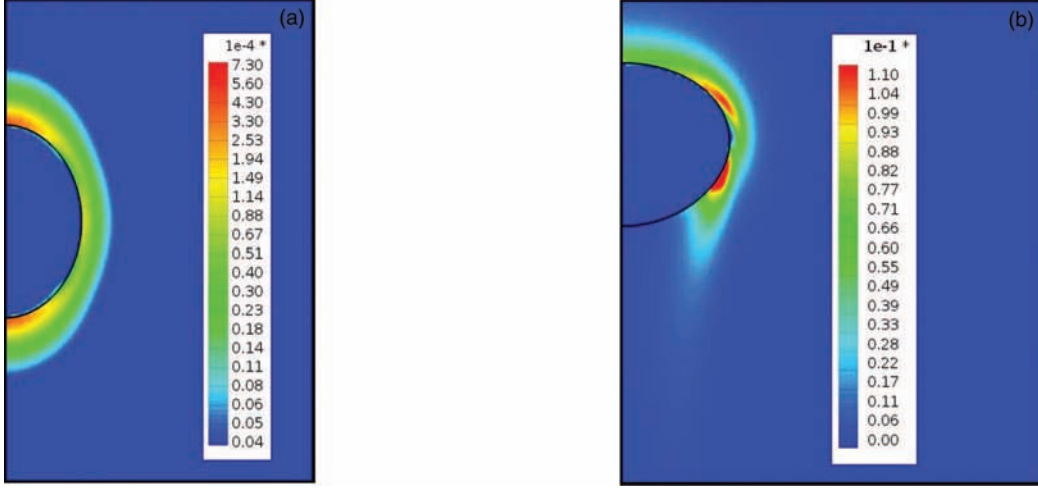


FIG. 16. Bubbles: Rate of dissipation normalized by $\rho_c(\omega_2^{th}R)^2\beta_2^{th}$ at time $t^* = 4T_2^{th} + 3T_2^{th}/4$ for $Re_{OSC} = 100$. (a) Case B_{0OSC} in the absence of gravity. (b) Rapidly rising bubble B_{FOSC} at $Bo = 1.050$ ($Re_\infty = 257$, $Re_{ASC}(t^*) = 246$).

shape. As the eigenvectors deviate more and more from the spherical harmonics, the oscillation, which was initially entirely conveyed by harmonic 2, is distributed over several harmonics. If this description is correct, the rate β_l at which the amplitude of each mode evolves should be prescribed by the average shape. Figure 15(b) shows the values of $\beta_2(t)/\beta_2^{th}$ for all cases and instants against the rate of change of $\langle \hat{a}_2 \rangle$ normalized by the damping rate of mode 2 in the absence of gravity: $\frac{1}{R\beta_2^{th}} \frac{d\langle \hat{a}_2 \rangle}{dt}$. All points nicely collapse on a master curve, which supports the proposed interpretation. It is remarkable that β_2/β_2^{th} reaches unity when the equilibrium bubble shape is steady. Even though the bubble rises fast, the damping rate of the final mode is close to the value in the absence of gravity.

C. Discussion of mechanisms

In this range of Reynolds numbers, both the shape oscillation and the rising motion of a bubble are mainly controlled by potential mechanisms. At $Re_{OSC} = 100$, the asymptotic development of Miller and Scriven⁶ for an oscillating bubble in the absence of gravity shows that 98% of the damping rate results from the dissipation within the potential flow. At $Re_{ASC} = 200$, Moore's calculation²⁵ shows that the potential flow contributes for 82% of the drag force of a spherical rising bubble. The predominance of the potential flow in the dissipation mechanism is illustrated in Fig. 16 where the rate of dissipation is plotted for oscillating bubbles at $Re_{OSC} = 100$. For a non-rising bubble (Fig. 16(a)), one notes that the maximum dissipation is located at the poles where the velocity normal to the interface is maximum. For a fast rising bubble (Fig. 16(b)), we observe that the dissipation is localized in the region of potential flow in front of and besides the bubble, whereas the contribution of the wake is negligible.

We consider now the different contributions of the mechanical energy. The potential energy of the surface that is associated with the bubble deformation, $E_{surf}(t) = \sigma(S(t) - 4\pi R^2)$, is calculated from the area $S(t)$ of the bubble interface at each instant t . The kinetic energy of the fluid, $E_{kin}(t)$, is calculated from the fluid velocity $U(r, z, t)$ by integration of $\frac{1}{2}\rho U^2$ over the computational domain. The work of gravity is obtained from time integration of the bubble rising velocity, $E_{grav}(t) = \frac{4}{3}\pi R^3 \Delta\rho g \int_0^t V(\tau) d\tau$ (with $\Delta\rho = \rho_c - \rho_d$). We will consider the five cases presented in Table VII: B_{0OSC} is the reference case of a bubble that oscillates in the absence of gravity; B_{SOSC} corresponds to a slowly rising bubble which remains almost spherical and for which β_2 remains always close to β_2^{th} ; B_{FOSC} is a rapidly rising bubble that deforms significantly; B_{SnoOSC} and B_{FnoOSC} are similar to B_{SOSC} and B_{FOSC} without initial deformation.

TABLE VII. Bubbles: Parameters of the selected cases for examination of the different contributions of the mechanical energy. In this table, t_∞ represents the steady state.

Bubble	Re_{OSC}	Bo	$a_2(t=0)/R$	Re_∞	We_∞	$\omega_2(t_\infty)/\omega_2^{th}$	$\beta_2(t_\infty)/\beta_2^{th}$	$\langle \chi \rangle(t_\infty)$
B_{0OSC}	100	0.000	0.075	0	0.0	1.0	1.0	1.0
B_{SOSC}	100	0.066	0.075	49	0.12	1.0	1.1	1.0
B_{SnoOSC}	100	0.066	0.000	49	0.12			1.0
B_{FOSC}	100	1.050	0.075	257	3.30	0.9	1.0	1.8
B_{FnoOSC}	100	1.050	0.000	257	3.30			1.8

In an attempt to reveal the dynamics of the shape oscillations, we have subtracted from each contribution of the mechanical energy ($E_{surf}(t)$, $E_{kin}(t)$, and $E_{grav}(t)$) of a rising and oscillating case (B_{SOSC} or B_{FOSC}) the same contribution of the corresponding non-oscillating case (B_{SnoOSC} or B_{FnoOSC}). The results are denoted $\Delta E_{surf}(t)$, $\Delta E_{kin}(t)$, and $\Delta E_{grav}(t)$ and compared to the values, $E_{surf}^0(t)$ and $E_{kin}^0(t)$, of the case without gravity B_{0OSC} .

Figure 17 shows the results for the slowly rising bubble. For these parameters, the energy associated with the rising motion is of the same order of magnitude as that associated with the oscillatory motion and the bubble shape remains spherical ($\langle \chi \rangle = 1.0$). The results show that ΔE_{grav} is negligible at all instants, $\Delta E_{surf}(t)$ matches $E_{surf}^0(t)$, and $\Delta E_{kin}(t)$ matches $E_{kin}^0(t)$. The oscillations of the rising bubble are thus similar to that of a non-rising bubble. The kinetic energy and the surface energy are in antiphase. In view of the fact that they are quadratic with respect to the amplitude, they are oscillating at $2\omega_2$ and decreasing as $\exp(-2\beta_2 t)$. Moreover, $\beta_2 \approx \beta_2^{th}$ because the oscillatory motion is not significantly altered by the rising motion.

Figure 18 shows the results for the rapidly rising bubble. In this case, the rate of dissipation of energy is two orders of magnitude higher than that of the non-rising bubble (Fig. 16). We observe that ΔE_{grav} remains small, which means that the oscillating and the non-oscillating bubbles rise almost

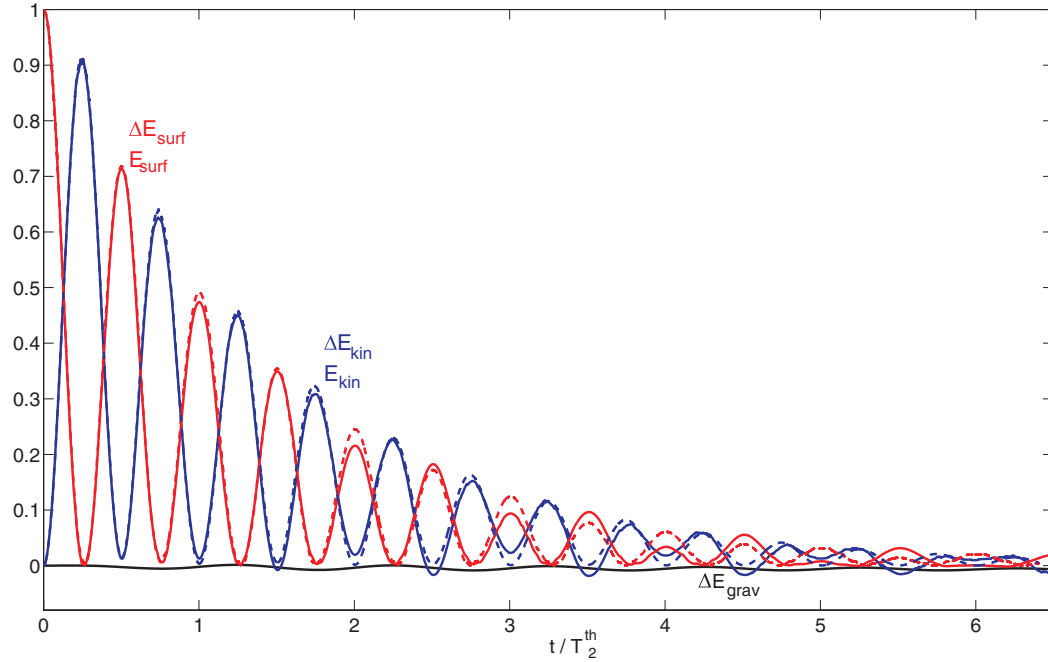


FIG. 17. Bubbles: Contributions to the mechanical energy of the shape oscillations normalized by the initial surface energy $E_{surf}(t=0)$. [—] $\Delta E_{surf}(t)$, $\Delta E_{kin}(t)$, and $\Delta E_{grav}(t)$ for the slowly rising bubble. [---] $E_{surf}^0(t)$ and $E_{kin}^0(t)$ for the non-rising bubble B_{0OSC} .

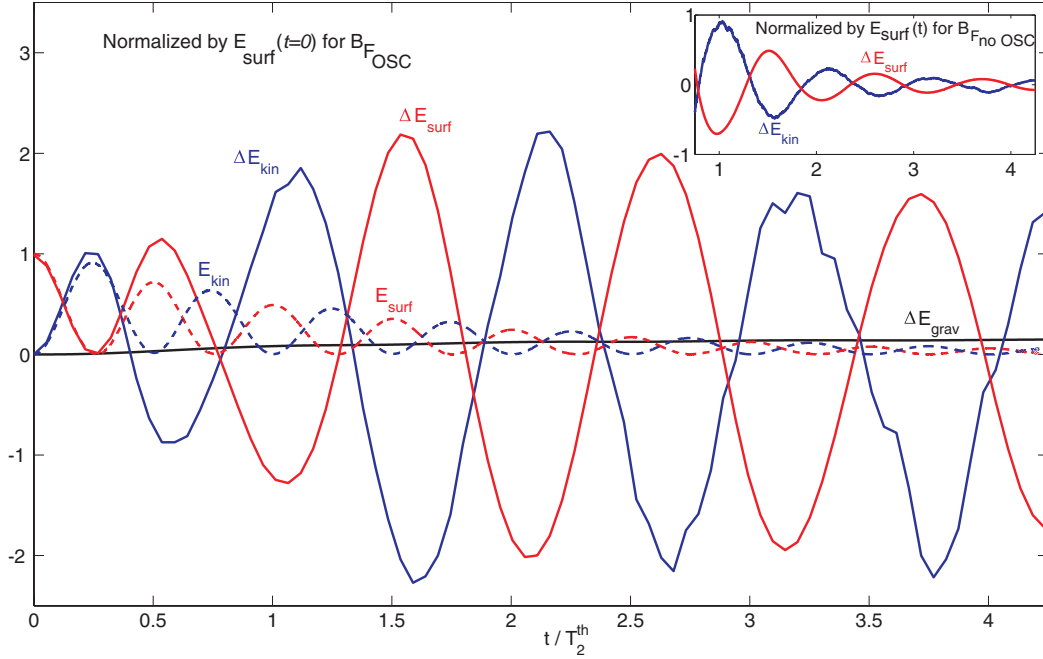


FIG. 18. Bubbles: Contributions to the mechanical energy of the shape oscillations normalized by the initial surface energy $E_{surf}(t=0)$. [—] $\Delta E_{surf}(t)$, $\Delta E_{kin}(t)$, and $\Delta E_{grav}(t)$ for the rapidly rising bubble. [- - -] $E_{surf}^0(t)$ and $E_{kin}^0(t)$ for the non-rising bubble B_{0OSC} . Inset: $\Delta E_{surf}(t)$ and $\Delta E_{kin}(t)$ normalized by the surface energy for the rapidly rising and non-oscillating bubble $B_{Fno OSC}$.

at the same velocity. $\Delta E_{surf}(t)$ and $\Delta E_{kin}(t)$ should thus be representatives of the energy associated with the oscillating motion. Their time evolution shows two different stages. During the first period of oscillation, the bubble is still almost spherical and $\Delta E_{surf}(t)$ and $\Delta E_{kin}(t)$ are similar to $E_{surf}^0(t)$ and $E_{kin}^0(t)$, like for the case of the slowly rising bubble. After the second period of oscillation, as the bubble deforms significantly, the period of oscillation of $\Delta E_{surf}(t)$ and $\Delta E_{kin}(t)$ doubles and their amplitude increases first significantly for eventually decaying at a rate close to β_2^{th} . $\Delta E_{surf}(t)$ and $\Delta E_{kin}(t)$, which are still in anti-phase and of similar amplitude, oscillate now around an almost zero average. The mechanical energy of the oscillation, which is the sum of the kinetic and the surface energy, is therefore no more related to their peak-to-peak amplitude. Let us compare the evolution of the surface energy for the oscillations around a spherical and a non-spherical bubble. For sake of simplicity, we only consider harmonic 2. Examine first the case of a sphere. Each time the amplitude a_2 vanishes the bubble is a sphere and the surface energy is minimum. Each time a_2 reaches a positive (prolate shape) or negative (oblate shape) extremum, the surface energy is maximum. The surface energy is therefore oscillating at twice the frequency of the amplitude a_2 . Examine now the case of an oblate equilibrium shape. Maximum surface energy is still reached when a_2 reaches its negative minimum since the bubble is then more oblate than the equilibrium shape. But minimum surface energy is now reached when a_2 reached its positive maximum, since the bubble is then less oblate than at the equilibrium, which corresponds to an intermediate deformation. The frequency of surface oscillation is therefore the same as the frequency ω_2 of amplitude a_2 . This is an original situation: the bubble experiences oscillations around a non-spherical equilibrium shape while the corresponding mechanical energy remains at each instant close to the surface energy of the equilibrium shape. Of course, (1) a non-spherical equilibrium shape and (2) a kinetic energy smaller than the value reached when the bubble passes by the equilibrium shape are possible because the bubble is rising. Such a behavior thus shows the limits of a description of the shape oscillation independently of the rising motion. Since $\Delta E_{surf}(t)$ and $\Delta E_{kin}(t)$ are not representative of the energy of the oscillation, it is not easy to draw conclusion from their rapid increase between 0.75 and $2T_2^{th}$. The inset of Fig. 18 shows their values normalized by the surface energy of the equilibrium shape, $E_{surf}(t)$ of case

$B_{F_{no\ OSC}}$. With this normalization, $\Delta E_{surf}(t)$ and $\Delta E_{kin}(t)$ show regularly damped oscillations with an initial amplitude close to unity. This suggests that their amplitude is controlled by the deformation of the average shape.

V. CONCLUDING REMARKS

The objective of this work was to determine the effect of the rising motion on the linear shape oscillations of drops and bubbles. We have computed the behavior of drops and bubbles that were initially deformed and released from rest in a liquid in the presence of gravity. As the bubble or drop rises, it is flattened by the action of hydrodynamic forces associated with the rising motion. Oscillations therefore no longer occur around a spherical equilibrium shape, which causes an evolution of the eigenmodes of oscillation. This is the major cause of the slight decrease of the oscillating frequency, which remains well predicted by the potential theory. When terminal shape and velocity are reached, a single mode that involves several spherical harmonics is present.

Two major differences between drops and bubbles have been observed. First, bubbles that have negligible mass experience larger accelerations. For similar oscillating and rising Reynolds numbers, bubbles deform more and faster. Also, owing to the variations of the added-mass coefficient, shape oscillations of bubbles cause much stronger velocity oscillations than those of drops. Second, the damping coefficient shows a totally different behavior. In the case of drops, the damping results from the dissipation within the boundary layers that develop on both sides of the interface. As the rising velocity increases, the boundary layers associated with the oscillating motion are affected by the boundary layers associated with the rising motion, and the damping rate increases. In the case of bubbles, the damping arises from the dissipation by the potential flow, which is weakly affected by the flow associated to the rising motion. At terminal velocity, the damping is close to the value in the absence of gravity.

We can now wonder what are the consequences of the rising motion on shape oscillations of drops or bubbles in practical situations.

For millimeter-sized drops of common fluids, the Weber number based on the rising velocity can hardly be larger than unity. The present results show that the deviations from the case without rising motion are low: less than 5% for the frequency and 20% for the damping rate. The well-known theoretical expressions obtained by assuming the absence of gravity therefore provide a good estimation of the interface timescales, which justified *a posteriori* their use for the prediction of the breakup probability in turbulent flows in Ref. 2. Nevertheless, it is worth mentioning that this is only true provided surface-active contaminants are absent, since they can increase three times the damping rate through a Marangoni effect.¹⁷

For bubbles at terminal velocity, the frequency – which is given by Meiron’s theory – and the damping rate are also weakly affected by the rising velocity. However, during transient stages when the equilibrium shape of the bubble is changing at a rate comparable to the oscillating frequency, complex and sudden changes in the amplitude of the spherical harmonics can be observed. This occurs when a deformed bubble is released from rest. That could also be the case when a bubble impacts a strong turbulent eddy. In a turbulent flow, the theoretical values obtained in the absence of gravity are therefore reliable to predict the relaxation of the shape after the interaction with a strong turbulent eddy. However, the response to this interaction is much more damped, in agreement to what has been observed in Ref. 18.

¹ F. Risso and J. Fabre, “Oscillations and breakup of a bubble immersed in a turbulent field,” *J. Fluid Mech.* **372**, 323–355 (1998).

² S. Galinat, F. Risso, O. Masbernat, and P. Guiraud, “Dynamics of drop breakup in inhomogeneous turbulence at various volume fractions,” *J. Fluid Mech.* **578**, 85–94 (2007).

³ R. Maniero, O. Masbernat, E. Climent, and F. Risso, “Modeling and simulation of inertial drop break-up in a turbulent pipe flow downstream of a restriction,” *Int. J. Multiphase Flow* **42**, 1–8 (2012).

⁴ P. J. O’Rourke and A. A. Amsden, “The TAB method for numerical calculation of spray droplet breakup,” SAE Tech. Pap. Ser. **218**, 872089 (1987).

⁵ H. Lamb, *Hydrodynamics* (Cambridge University Press, Cambridge, 1932).

⁶ C. A. Miller and L. E. Scriven, “The oscillations of a fluid droplet immersed in another fluid,” *J. Fluid Mech.* **32**, 417–435 (1968).

- ⁷P.-L. Marston, "Shape oscillation and static deformation of drops and bubbles driven by modulated radiation stress – Theory," *J. Acoust. Soc. Am.* **67**, 27 (1980).
- ⁸A. Prosperetti, "Normal mode analysis for the oscillations of a viscous liquid drop in an immiscible liquid," *J. Mec.* **19**, 149–182 (1980).
- ⁹I. S. Kang and L. G. Leal, "Bubble dynamics in time-periodic straining flows," *J. Fluid Mech.* **218**, 41–69 (1990).
- ¹⁰A. Prosperetti, "Free oscillations of drops and bubbles: The initial-value problem," *J. Fluid Mech.* **100**, 333–347 (1980).
- ¹¹J. A. Tsamopoulos and R. A. Brown, "Nonlinear oscillations of inviscid drops and bubbles," *J. Fluid Mech.* **127**, 519–537 (1983).
- ¹²H. Azuma and S. Yoshihara, "Three-dimensional large-amplitude drop oscillations: Experiments and theoretical analysis," *J. Fluid Mech.* **393**, 309–332 (1999).
- ¹³O. A. Basaran, "Nonlinear oscillations of viscous liquid drops," *J. Fluid Mech.* **241**, 169–198 (1992).
- ¹⁴T. Watanabe, "Numerical simulation of oscillations and rotations of a free liquid droplet using the level set method," *Comput. Fluids* **37**, 91–98 (2008).
- ¹⁵E. Becker, W. J. Hiller, and T. A. Kowalwski, "Experimental and theoretical investigation of large-amplitude oscillations of liquid droplets," *J. Fluid Mech.* **231**, 189–210 (1991).
- ¹⁶T. G. Wang, A. V. Anilkumar, and C. P. Lee, "Oscillations of liquid drops : Results from USML-1 experiments in space," *J. Fluid Mech.* **308**, 1–14 (1996).
- ¹⁷N. Abi Chebel, J. Vejražka, O. Masbernat, and F. Risso, "Shape oscillations of an oil drop rising in water: Effect of surface contamination," *J. Fluid Mech.* **702**, 533–542 (2012).
- ¹⁸F. Ravelet, C. Colin, and F. Risso, "On the dynamics and breakup of a bubble rising in a turbulent flow," *Phys. Fluids* **23**, 103301 (2011).
- ¹⁹D. I. Meiron, "On the stability of gas bubbles rising in an inviscid fluid," *J. Fluid Mech.* **198**, 101–114 (1989).
- ²⁰S. V. Subramanyam, "A note on the damping and oscillations of a fluid drop moving in another fluid," *J. Fluid Mech.* **37**, 715–725 (1969).
- ²¹S. Tanguy, T. Ménard, and A. Berlemont, "A level set method for vaporizing two-phase flows," *J. Comput. Phys.* **221**, 837–853 (2007).
- ²²S. Tanguy and A. Berlemont, "Application of a level-set method for simulation of droplet collisions," *Int. J. Multiphase Flow* **31**, 1015–1035 (2005).
- ²³M. Sussman, K. M. Smith, M. Y. Hussaini, M. Ohta, and R. Zhi-Wei, "A sharp interface method for incompressible two-phase flows," *J. Comput. Phys.* **221**, 469–505 (2007).
- ²⁴R. Mei, J. F. Klausner, and C. J. Lawrence, "A note on the history force on a spherical bubble at finite Reynolds number," *Phys. Fluids* **6**, 418–420 (1994).
- ²⁵D. W. Moore, "The boundary layer on a spherical gas bubble," *J. Fluid Mech.* **16**, 161 (1963).
- ²⁶T. Bonometti and J. Magnaudet, "An interface capturing method for incompressible two-phase flows: Validation and application to bubble dynamics," *Int. J. Multiphase Flow* **33**, 109–133 (2007).
- ²⁷A. Blanco and J. Magnaudet, "The structure of the axisymmetric high Reynolds number flow around an ellipsoidal bubble of fixed shape," *Phys. Fluids* **7**, 1265 (1995).
- ²⁸J. Gordillo, B. Lalanne, F. Risso, D. Legendre, and S. Tanguy, "Unsteady rising of clean bubble in low viscosity liquid," *Bub. Sci. Eng. Tech.* **4**, 4–11 (2012).
- ²⁹D. W. Moore, "The velocity of rise of distorted gas bubbles in a liquid of small viscosity," *J. Fluid Mech.* **23**, 749 (1965).
- ³⁰J. de Vries, S. Luther, and D. Lohse, "Induced bubble shape oscillations and their impact on the rise velocity," *Eur. Phys. J. B* **29**, 503–509 (2002).
- ³¹T. B. Benjamin, "Hamiltonian theory for motion of bubbles in an infinite liquid," *J. Fluid Mech.* **181**, 349–379 (1987).
- ³²D. Legendre, R. Zenit, and J. R. Velez-Cordero, "On the deformation of gas bubbles in liquids," *Phys. Fluids* **24**, 043303 (2012).